Author Version of : Marine Geology, vol.459; 2023; Article no: 107046

A 50 kyr Record of Eolian Sedimentation in the Eastern Arabian Sea –Dust deposition changes synchronous with the Northern Hemisphere Climatic Oscillations

Tyson Sebastian[1,2], B. Nagender Nath[1]*, M.B.L. Mascarenhas-Pereira[1], M. Venkateshwarlu[3], Tanvi Mungekar[1], Dryden Joe Rodrigues[1], Suresh K.[1], Linsy P.[1,2]

[1]CSIR- National Institute of Oceanography, Dona Paula, Goa, India, 403004

[2]National Centre for Polar and Ocean Research, Goa, India, 403804

[3]CSIR – National Geophysical Research Institute, Uppal Road, Hyderabad, India, 500007

*Corresponding author email: nagendernath@yahoo.com

Abstract

The Late Pleistocene Northern Hemisphere (NH) climate was extremely variable, owing to the abrupt warm Dansgaard–Oeschger (D/O) events and cold Heinrich events in the Greenland and North Atlantic. Although the close coupling between the Indian monsoon and the Northern hemisphere climatic fluctuations has been previously reported from several western and northern Arabian Sea records, these millennial-scale climatic oscillations are not clearly defined in the Eastern Arabian Sea (EAS) possibly because many of the past records are from the continental margin which are vulnerable to sediment slumps and slides. Here, we present a 50 kyr eolian sedimentation record from a bathymetric high off Goa in the EAS, reconstructed using the environmental magnetic parameter S-ratio (a measure of the relative proportions of ferromagnetic and canted antiferromagnetic minerals) and the mass accumulation rate of iron and magnesium (Fe_{MAR} and Mg_{MAR}). S-ratio record shows striking similarity with the $\delta^{18}O$ record from the Greenland GISP2 ice core, indicating the control of the temperature fluctuations of high northern latitudes on the low-latitude climate variability. The cold Heinrich events are marked by lowered S-ratios indicating less eolian input while the D/O interstadials are marked by increased S-ratios illustrating the intensified summer monsoon wind strength and the increased eolian supply during these periods. The mass accumulation rate of Mg and Fe reveals high values during 29 - 18 kyr reflecting the increased source area aridity and dust transport during the last glacial period. The spectral analysis of the S-ratio record reveals significant periodicities centered at 24 kyr and 1.3 kyr establishing the orbital and northern hemisphere controls on the EAS climate.

Keywords: Dust deposition, Dansgaard–Oeschger events, S-ratio, monsoonal winds, Source area aridity, Heinrich events, Bathymetric Highs.

1. Introduction

The Late Pleistocene climate is marked by large, rapid, millennial-scale variations termed as Dansgaard/Oeschger (D/O) and Heinrich events over Greenland and North Atlantic (Dansgaard et al., 1993; Heinrich, 1988). The time equivalents of these abrupt events have been identified from a number of high resolution climate records from both northern (Allen et al., 1999; Benson et al., 1998; Cacho et al., 1999; Peterson et al., 2000; Porter and Zhisheng, 1995) and southern (Arz et al., 1998; Bender et al., 1994; Charles et al., 1996) hemispheres. The close linkage of D/O oscillations with monsoonal precipitation (Leuschner and Sirocko, 2000; Deplazes et.al.,2014), denitrification and upwelling (Altabet et al., 2002), primary productivity (Schulte and Müller, 2001; Schulz et al., 1998), wind strength and deposition (Pourmand et al., 2004) have been previously reported from several Arabian Sea records. Indian summer monsoon shifts during D/O events were also tracked using speleothem records from Moomi Cave, Socotra Island, western Arabian Sea (Burns et al., 2003) and Mamwluh cave, northeastern India (Jaglan et al., 2021). However, these studies are concentrated on the Western and Northern Arabian Sea and there are only a few records from the Eastern Arabian Sea (EAS) discussing the forcing of D/O oscillations on the pteropod preservation (Singh, 2021), denitrification (Nagoji and Tiwari, 2021) and the diameter of planktic foraminifer *Orbulina universa* (Nimmy et al., 2021).

The EAS is a region of complex interplay between several spatially and temporally varying oceanographic processes such as coastal upwelling (Wyrtki, 1971) and seasonal hypoxia (Naqvi et al., 2000) during the SW monsoon which have the potential to impact the basin-scale oceanography (Narvekar et al., 2017). Besides this, the EAS receives significant amount of eolian material via wet deposition (through rainfall) (average annual wet deposition over Goa, a coastal state in the west coast of India - 20.7 g m^{-2}, Ramaswamy et al., 2017, **Fig. 1**) through the SW monsoon winds (Suresh et al., 2021). This mineral dust and aerosols also supply micronutrients like iron (~1.4 $gm^{-2}a^{-1}$; Ramaswamy et al., 2017) and additional soluble nutrients like phosphorous and nitrogen which can contribute substantially to oceanic primary productivity and biogeochemical processes (Jickells et al., 2005; Banerjee and Kumar, 2014; Bali et al., 2019). In the NW Arabian Sea, the late Quaternary records of grain size, flux and mineralogy of the dust have been used to evaluate the environmental conditions in the source areas and the potential association between the dust deposition and upwelling systems (Krissek and Clemens, 1992). However, the eolian sedimentation history has been poorly documented in the EAS owing to the lack of long-term sedimentary records with limited interference from fluvial sedimentation. Here we show, from the environmental magnetic and geochemical proxies, that the sediment cores from the flat-topped bathymetric highs from the

continental margin in EAS can act as excellent archives of long-term records of eolian sedimentation and present a 50 kyr record of eolian sedimentation and its linkage to regional climatic changes

2. Materials and methods

2.1. Study area and sampling

The Arabian Sea is a low-latitude sea in the Indian Ocean and is under the marked continental influence from the northern, eastern, and western sides by the landmasses of Asia and Africa. The differential heating and cooling between the Tibetan Plateau/Indian subcontinent and the surrounding Indian Ocean results in the seasonal reversal of wind and surface water circulation. These seasonally reversing winds (Webster, 1987) bring monsoon (southwest monsoon from June - September and northeast monsoon from December - March) to the Indian subcontinent and cause upwelling along the continental margins of India. This intense upwelling and the limited bottom water ventilation due to the mostly land-locked nature of the Arabian Sea results in a strong mid water oxygen minimum zone (OMZ) between the water depths of 200 to 1200 meters (Wyrtki, 1973).

The southwestern continental margin of India between latitudes 12 and 15 degrees north has several flat topped NNW - SSE trending bathymetric highs (Rao et al., 2010; Bijesh et al., 2018). They occur between 245 to 1600 m water depths and form a chain of horst and graben structures covered by thick sediments (Rao et al., 2010). A gravity core labeled SSK80/GC2 of 150 cm length (hereafter referred as GC2) was collected from a water depth of 331 meters on a bathymetric high off Goa, Eastern Arabian Sea (14.76°N, 72.67°E) with basal depths of 1200 m in the landward side and 1550 m in the seaward side located 140 km away from the nearest coast **(Fig. 1)**.

2.2. Chronology

The chronology of the core was constructed using eight calibrated ^{14}C dates obtained from the analysis of mixed planktic foraminifera (*Globigerinoides ruber* and *Globigerinoides sacculifer)* at NSF-Arizona AMS Laboratory, USA and Radiochronology Lab, Laval University, Canada. Bulk sediment samples from eight depths were wet-sieved using 125 μm mesh and the retained fraction was dried. Approximately 10 mg of clean foraminiferal specimens were handpicked from this fraction and used for the AMS ^{14}C dating. The measured radiocarbon ages were converted into calendar years using CalPal 2007 program (http://www.calpal.de) after applying a reservoir correction of 400 years (Govil and Naidu, 2010) which falls in the range of values (315 to 474 years compiled by Dutta, 2008) used for Bay of Bengal. The details of the chronological analyses with lab reference numbers and calibrated ages are presented in **Table 1**.

2.3. Oxygen isotope measurements

The oxygen isotope analysis was performed on 8 to 12 tests of planktic foraminifera *G. ruber*. The well-preserved tests which showed no dissolution and contamination were picked from the coarse fraction (>125 μm) of 72 samples (from different subsurface depths) under a stereo zoom binocular microscope and were cleaned by keeping in an ultrasonic bath. The oxygen ($\delta^{18}O$) isotopic measurements were carried out on these tests using a Delta-Plus continuous flow Isotope Ratio Mass Spectrometer (IRMS) coupled with a Kiel IV automatic carbonate device at the CSIR-NIO, Goa. The accuracy of the measurements was ensured using the international carbonate standards Carrara Marble Powder and NBS 19.

2.4. Environmental magnetic analyses

The environmental magnetic concentration, grain size and mineralogical parameters were measured on freeze dried samples (~ 4g) at 1 cm interval (n=148) at CSIR – NGRI, Hyderabad, India (for more details on magnetic parameters and their description, refer Sebastian et al., 2019). Low (0.47 kHz) and high (4.7 kHz) frequency magnetic susceptibility (χ_{lf} and χ_{hf}) measurements were carried out using a Bartington MS2B sensor and the frequency dependent susceptibility (χ_{fd}) was calculated by the equation (Dearing et al., 1996),

$$\chi_{fd}\% = [(\chi_{lf} - \chi_{hf})/\chi_{lf}] \times 100 \qquad (1)$$

Anhysteretic remnant magnetization (ARM) was imparted to the sample by a 100 mT peak alternating feld and a 0.05 mT constant bias feld using a Molspin AF demagnetizer and was measured using a JR-6 dual speed spinner magnetometer (AGICO, Czech Republic). The susceptibility of ARM (χ_{arm}), a magnetic concentration parameter, was calculated by dividing the obtained ARM values with the weight of the sample. The saturation isothermal remnant magnetization (SIRM) parameter was measured at a pulse field of 1T followed by IRM measurements at reverse fields of -20, and -300 mT respectively. The S-ratio, a measure of the relative abundance of ferrimagnetic and antiferromagnetic minerals, was calculated using the equation,

$$\text{S-ratio} = IRM_{-300mT}/SIRM \qquad (2)$$

2.5. Geochemical analyses

Geochemical analyses were carried out using Inductively Coupled Plasma – Optical Emission Spectroscopy (ICP – OES) and Mass Spectroscopy (ICP – MS) techniques at CSIR - NIO, Goa, India. Powdered sediment samples (50 mg) at 1 cm interval (n=148) were digested using an acid

mixture (7:3:1 - HF: HNO_3: $HClO_4$) in Teflon beakers and final solution was prepared in 4% HNO_3. Fe, Mg, and Al content in the samples were measured ICP- OES (PerkinElmer Optima 7300 DV) and Ti content was measured using ICP-MS (Thermo Scientific, XSERIES 2, Quadrupole). The analytical accuracy and precision were determined using the reference material MAG -1 (United States Geological Survey) and the replicate measurements respectively and the accuracy and precision were within ±2%. The mass accumulation rate of iron (Fe_{MAR}) and magnesium (Mg_{MAR}) were calculated by multiplying the elemental concentration, sedimentation rate and dry bulk density of the samples.

2.6. Grain-size measurements

Seventy-five alternately spaced sediment samples of 1 cm thickness, approximately 4 g in weight, were wet sieved using 63 µm mesh and the fraction retained on sieves was separated. The >63 µm fraction was mostly composed of biogenic carbonates. The <63 µm fraction was treated using acetic acid and hydrogen peroxide to remove calcium carbonate and organic carbon respectively. This has helped separate the aggregates. Following this, the suspension was sonicated using an Ultrasonic bath. This fraction representing silt+clay size was then analyzed with Laser Particle Size Analyzer (LPSA) (Malvern Mastersizer 2000) to determine the texture of this lithogenic fraction. The median grain size (D_{50}) of this silt+clay lithogenic fraction was calculated from the data.

3. Results

3.1. AMS ^{14}C dates and sedimentation rates

The results from the ^{14}C dating yielded an age of 46 ka BP for 140 – 141 cm section with the average sedimentation rate working out to 3.14 cm/kyr **(Fig. 2, Table 1)**. Highest sedimentation rates (4.5 and 8.23 cm/kyr) are recorded during MIS 2 (29 – 18 ka) while lowest sedimentation rates (~ 1.3 and 1.8 cm/kyr) are seen during MIS 3 (40 – 29 ka) and last glacial maximum (LGM) to mid-Holocene (18 – 6 ka) respectively. An increase in sedimentation is evident in the mid- to late-Holocene period (~ 4.5 cm/kyr) **(Fig. 2)**.

3.2. Oxygen isotopic variations

The δ^{18}O measurements of *G. ruber* in GC 2 **(Fig. 3)** show values between -0.46 and -3.1 ‰ over the last 50 kyr (**Supplementary data file**). Lighter values are seen during Holocene (average – -2.4 ‰) compared to MIS 2 (-1.22 ‰) and MIS 3 (-1.36 ‰) suggesting wetter conditions during Holocene, while heaviest values are observed during MIS 2. Major climatic periods such as LGM

and YD in GC 2 are clearly comparable to GISP2 $\delta^{18}O$ record (Grootes and Stuiver, 1997) **(Fig. 3)**.**3.3. Magnetic mineral concentration, grain size and mineralogy**

All the environmental magnetism data is presented in **Supplementary data file**. The downcore variation of magnetic concentration and mineralogical parameters are shown in **Fig. 4**. The concentration parameters χ_{arm} and SIRM vary between 0 – 2.9 (average – 0.52, unit – 10^{-5} m^3kg^{-1}) and 30 – 1170 (average – 244, unit – 10^{-5} Am^2kg^{-1}) respectively with highest values during mid- to late-Holocene. The parameters show a decreasing trend downcore and the values become close to zero in MIS 3. Magnetic mineralogical parameter S-ratio also shows a decreasing downcore trend with high values in MIS 1 and low values in MIS 2 and MIS 3. The values range between 0.64 and 0.97 with an average value of 0.83 **(Fig. 4)**. The bi-plot of χ_{fd}% vs χ_{arm}/SIRM is an indicator of the magnetic grain size (Dearing et al., 1997; Maher, 1998). In the core GC2, the sediments deposited during MIS 1 and MIS 2 periods fall in the 'stable single domain/superparamagnetic (SSD/SP) transition and fine SSD' fields while the samples from MIS 3 plot on the 'coarse SSD' field **(Fig. 5)**. S-ratio is a measure of the relative concentration of low coercivity ferrimagnetic minerals such as magnetite and maghemite to the high coercivity antiferromagnetic minerals such as hematite and goethite. The values close to the unity indicate the dominance of ferrimagnetic minerals and lower values indicate the dominance of antiferromagnetic minerals (Thompson and Oldfield, 1986).

3.4. Major element geochemistry

The major element data too is presented in **Supplementary data sheet** and **Fig.3**. Fe and Mg content in the core vary between 0.6 – 2.16 wt.% and 0.6 – 1.54 wt.% respectively. Refractory elements Ti and Al range between 0.06 and 0.24 wt.% and 0.93 and 3.11 wt.% respectively. Elemental concentrations display three periods of increase during 0 – 6 kyr, 18 – 26 kyr and 44 – 50 kyr **(Fig. 3)**.

3.5. Textural characteristics

Textural data is presented in **Supplementary Data File.** The >63 μm size fraction representing sand is the dominant fraction in this core and range between 30 - 85 wt.% with an average of 60 wt.%. The sand is mostly composed of biological skeletal components. The highest values are seen during late Holocene while the lowest values are observed during 48 – 45 kyr (**Fig. 6**). In the <63 μm fraction, clay content varies between 43 – 79 wt.% with an average value of 69 wt.% while the silt content range between 23 – 56 wt.% with an average of 31 wt.%. A higher silt content is observed during the mid- to late-Holocene period (6 – 0 ka) with minor changes in the rest of the core (**Fig. 6**). The median grain size (D_{50}) varies between 3 and 7.2 μm (average – 3.80 μm),

with comparatively higher median values during mid- to late-Holocene and 35 – 25 ka period **(Figs.3 & 6)**.

4. Discussion

The sediment core GC2 location is situated on a bathymetric high off Goa, EAS, with a summit depth of 305 m and a basal depth of 1200 m in the landward side and 1550 m in the seaward side **(Fig. 1)** (Rao et al., 2010). This topographically isolates the bathymetric high from the bedload and lateral fluvial sedimentation. The lack of major rivers in the adjoining coastal areas in the region and a 140 km distance from the sample location to the nearby coast limits the suspended fluvial contribution to the core site. Therefore, the eolian material constitutes the possible primary source of sediments to the core location. This is also evidenced from the very low sedimentation rate at the GC2 location compared to the nearby records (which are not on the topographic highs). The average sedimentation rate during Late Holocene and LGM in the Eastern Arabian Sea between Goa and Mangalore was reported to be 10 - 20 cm/kyr (Singh et al., 2017). A nearby sediment record (SK-17, 15.25°N, 72.96°E, water depth 640 m; Singh et al., 2011) reported an average sedimentation rate of 16.5 cm/kyr for the last 30 kyr. In comparison, the average sedimentation rates of this core (GC2) for the last 50 kyr are 3.14 cm/kyr and 5.2 cm/kyr for the late Holocene which are much lower than the areas with fluvial input. A comparable sedimentation rate (3.8 cm/kyr) was reported for a short sediment core (SSK40/SPC1R) from this same topographic high (Linsy et al., 2018). A single channel seismic reflection section (A-A') across the bathymetric high **(Fig. 1)** shows that only a thin layer of sediments exists on top of the high [two-way travel-time, (TWT) ~ 1.3s] compared to its eastern basin (TWT ~ 3.5s at ~1000 m water depth) (Chaubey et al., 2002; Rao et al., 2010). Eolian material which originate from the deserts in India, Pakistan, Iran, Iraq, the Arabian Peninsula, and the Horn of Africa is delivered to the Arabian Sea predominantly through the SW monsoon Low Level Jet and NW Shamal winds (Sirocko and Lange, 1991, Suresh et al., 2021) with an annual dust flux of 30 - 115 x 10^6 metric tons per year (Clemens, 1998). Eolian material was found to be dominating the terrigenous fraction of sediments in other bathymetric highs in the Western and Northern Arabian Sea too (Debrabant et al., 1991, Reichart et al., 1997) and was used to reconstruct the eolian sedimentation history (Clemens and Prell, 1990; Krissek and Clemens, 1992; Sirocko and Lange, 1991; Prins and Weltje 1999; Pourmand et al., 2004).

4.1. Environmental magnetic proxies of mineral dust deposition

The environmental magnetic measurement of the core GC2 shows high S-ratio (average - 0.93) in the top 24 kyr (MIS 1 and 2) while it encounters a drastic decrease in the MIS 3 (0.76) **(Fig.**

4). S-ratio values close to unity in MIS 1 and 2 indicate the abundance of ferrimagnetic minerals while the low values in MIS 3 suggest the increasing contribution from antiferromagnetic minerals (Thompson and Oldfield, 1986). The magnetic grain size bi-plot of χ_{fd}% vs χ_{arm}/SIRM **(Fig. 5)** suggest the presence of fine-grained magnetic grains in the MIS 1 and 2 with 'stable single domain/superparamagnetic' and 'fine SSD' grain sizes while MIS 3 samples are 'coarse SSD' sized grains. The grain size parameters and the S-ratio together suggest that the magnetic grain size coarsens down core and MIS 1 & 2 of the core is composed of ultrafine stable single domain ferrimagnetic grains.

The rapid decrease of S-ratio at the end of MIS 2 (~ 24 ka) indicates the diagenetic dissolution of fine grained biogenic and terrigenous magnetic minerals. This is also evident from the near-zero values of magnetic concentration parameters χ_{arm} and SIRM **(Fig. 4)**. Although the dissolution of magnetic minerals is considered as a bane in environmental magnetic studies of many depositional settings where it destroys the original paleoclimatic information carried by the terrigenous minerals (Karlin, 1990; Rowan et al., 2008), it could provide important clues of changes in depositional environment in some cases such as in this study. The diagenetic dissolution and the subsequent removal of the fine grained ferrimagnetic minerals such as magnetite can actually enhance the detrital magnetic signal, if, some or all of the fine-grained ferrimagnetic material in the affected zone is of authigenic or biogenic origin (Bloemendal et al., 1993). The environmental magnetic parameters and their ratios in the core GC2 suggest the presence of bacterial magnetite in the top 18 ka of the core. The values of magnetic ratios χ_{ARM}/SIRM $>200x10^{-5}mA^{-1}$ and χ_{ARM}/χ_{LF} $>40x10^{3}$ **(Fig. 4)** are indicators of the presence of bacterial magnetism (Oldfield, 1991; Walden, 1999). The average values of these ratios in the 24 - 0 ka period are 216.0 x 10^{-5} mA^{-1} and 71.6 x 10^{3} respectively. For the remaining part of the core (50 - 24 ka), the values are 71.6 x 10^{-5} mA^{-1} and 12 x 10^{3} respectively, showing the absence of biogenic magnetite in MIS 3 **(Fig. 4)**. The Field Emission Scanning Electron Microscopy (FE-SEM) analysis of the magnetic extracts from the core GC2 revealed the presence of stable single domain (SSD) sized magnetite grains of possible biogenic origin along with multi domain sized titanomagnetite grains of detrital origin **(Fig. 7)**. The diagenetic dissolution in the MIS 3 of the GC2 core seems to have dissolved the fine-grained biogenic magnetite grains but not affecting the coarse grained detrital titanomagnetite grains allowing the preservation of original paleoclimatic signal. A change from a predominantly SSD ferrimagnetic grains in MIS 1 and 2 to the coarser SSD grains in MIS 3 is a manifestation of this selective dissolution as reflected in the magnetic grain-size sensitive bi-plot of χ_{FD}% vs χ_{ARM}/SIRM **(Fig. 5)**.

4.2. Synchronous changes of EAS dust deposition, WAS monsoonal changes and the N. Atlantic climate

The S-ratio record of GC2 in the MIS 3 reveals large millennial-scale oscillations and show striking similarities with the $\delta^{18}O$ record from the Greenland GISP2 ice core (Grootes and Stuiver, 1997), indicating the control of the rapid temperature fluctuations of high northern latitudes on the low-latitude climate variability **(Fig. 8)**. The GC2 S-ratio record also agrees well with the total organic carbon (TOC) record from the Western Arabian Sea, an indicator of monsoon-induced productivity, and is strongly synchronous with Dansgaard–Oeschger and Heinrich events (Schulz et al., 1998). The optimal location of the GC2 record allowed the S-ratio to be used as a qualitative proxy for the eolian input over time, owing to the limited contribution from other sediment sources to the study area. Previous studies have successfully utilized S-ratio as a proxy for dust input in other basins such as Mediterranean Sea (Dinarès-Turell et al., 2003) and Burial Lake, Arctic Alaska (Dorfman et al., 2015). In the GC2 record, the cold Heinrich events are marked by lowered S-ratios indicating lowered eolian input while the D/O interstadials are marked by increased S-ratios illustrating the increased eolian supply during these periods **(Fig. 8)**. A 110 ka sedimentary record (93KL) from northeastern Arabian Sea by Pourmand et al., (2004) utilized ^{230}Th-normalized ^{232}Th fluxes as a proxy for detrital flux (of eolian origin) and found high dust input during Younger Dryas, Heinrich events and D/O stadials **(Fig. 8)**. The inverse relationship between the northeastern Arabian Sea dust record and GC2 record could be explained by the differences in the sources and the mode of deposition. The NE Arabian Sea receives the eolian input from the Arabian Peninsula and Persian Gulf region through the northwesterlies which are strongest between the summer and winter monsoon seasons (Pourmand et al., 2004). The high dust fluxes in the 93KL record during the cold events were attributed to the weakened southwest monsoon in conjunction with strengthened northwesterlies (Pourmand et al., 2004). In the EAS on the other hand, the modern observations suggest that the moist oceanic Low-Level Jet (Findlater Jet) of the SW monsoon, loaded with large quantities of dust from NE Africa and the Middle-East through the overriding Red Sea Wind and Shamal Wind, constitute the major contributor of eolian input (Ramaswamy et al., 2017). The annual deposition rate of mineral dust over Goa was found to be 2 to 5 times higher than those measured by sediment traps over the western and central Arabian Sea with the maximum deposition during the months of June and July. Thus, the increased S-ratios during the D/O interstadials in the GC2 record illustrate the strengthened SW monsoon winds during those periods which brought more eolian material to the EAS.

4.3. Major elements and lithogenic grain size tracking dust deposition

To quantitatively understand the dust deposition in the EAS, the mass accumulation rate (MAR) of iron (Fe_{MAR}) and magnesium (Mg_{MAR}) were calculated **(Fig. 9)**. In fluvially limited environments, such as our location, the dominant external input of iron is through aeolian dust transport (Jickells et al., 2005). The Mg distribution pattern in the Arabian Sea shows a persistent maximum in the western Arabian Sea as a result of dolomite - palygorskite rich dust discharge by the northern branch of the Arabian northwesterlies during summer (Sirocko et al., 2000). A very strong positive correlation is observed between Al and Fe (R^2 = 0.88, n = 147) and Al and Mg (R^2 = 0.82) respectively in our record suggesting their lithogenous association. The Fe and Mg MAR records reveal high values during 18 - 29 kyr along with the lesser prominent peaks during 2 - 6 kyr and 40 - 50 kyr. The MAR records of diagnostic elements have been utilized by many workers as a proxy for continental aridity (more dust reflects drier source regions), while the median grain size has been utilized to reconstruct the wind strength (larger grains reflects stronger winds) (Clemens and Prell, 1990; 1991; Rea, 1994). The high MAR of Fe and Mg during the 29 - 18 kyr correlates positively with the increased global ice volume (Gowan et al., 2021; **Fig. 9**) and reduced solar insolation (Berger and Loutre, 1991; **Fig. 10**) suggesting the increased eolian flux due to the arid conditions in the source regions during the last glacial period. Ti/Al ratio, a proxy for the relative contribution of eolian and fluvial sources (Shimmield et al., 1990; Schnetger et al., 2000) also record high values during this period confirming the increased dust input **(Fig. 9)**. This period is also marked with the high Mg/Al values in a nearby sediment record (15.48°N, 71.01°E; SK117/GC08) and was interpreted as a proxy for dust influx (Mir et al., 2022, **Fig. 9**). Sirocko et.al. (1996) have found Mg content to reflect changes in dolomite-and palygorskite-rich summer dust discharge by northwesterlies from north Arabia. Similar increase in the mass accumulation rate of lithogenic material (mainly eolian) during glacial periods was observed in the sediment record from the Owen Ridge, Western Arabian Sea (Clemens and Prell, 1991, 1990; **Fig. 9**) and was interpreted to reflect the effect of global climate on the source area aridity and vegetation cover, resulting in maximum dust transport during glacial intervals (Krissek and Clemens, 1992). This is also comparable to the records of relative amount of lithogenic dust from the Central Arabian Region derived by the first principal component (PC1) from the geochemical record of core 70KL (Leuschner et al., 2004), and continental aridity derived from the end-member modelling of siliciclastic grain-size distribution of NIOP458 from the Upper Indus fan (Prins and Weltje, 1999) **(Fig. 10)**.

The lithogenic median grain size of sediments has been employed as a proxy for the Indian summer monsoon (ISM) wind strength in the Arabian Sea by previous workers (Clemens and Prell,

1990, 1991 and the references therein). The median grain size (D_{50}) of GC2 varies between 3 – 7 μm with the highest values (average – 5.4 μm) during the late Holocene (5 – 2 kyr) suggesting the strengthening of SW monsoon winds **(Fig. 10)**. This agrees with the eolian mean grain size record of NIOP492 from Owen Ridge which records coarser grain size in the Holocene (Prins and Weltje 1999) **(Fig. 10)**. The Holocene strengthening of the ISM, though with multimillennial-scale fluctuations, has been documented by many workers (Thamban et al., 2001; Agnihotri et al., 2003; Clift et al., 2008; Miriyala et al., 2017; Sebastian et al., 2023). Median grain size shows finer values during LGM as opposed to the high MAR indicating the weakening of ISM wind strength during glacials. The increased MAR of Fe and Mg during 50 – 40 kyr period is also similar to the Mg/Al record of EAS (Mir et al., 2022) and lithogenic MAR record from the Owen Ridge (Clemens and Prell, 1990) suggesting an increase in dust flux during this period. The S-ratio record of this core and the eolian mean grain size record from Owen Ridge (Prins and Weltje 1999) also shows high values during 50 – 45 kyr supporting this interpretation.

4.4. Periodicity in dust deposition

A spectral analysis was carried out on the S-ratio and D_{50} records to better understand the northern hemisphere and solar controls on the EAS climate using the Lomb-Scargle Fourier transform package REDFIT (Schulz and Mudelsee, 2002), which determines the periodicity of an unevenly spaced data. The spectral analysis revealed statistically significant (95% significance level) periodicities centered at 24240 yr, 1273 yr and 757 yr for S-ratio and 12810 yr, 2865 yr and 1433 yr periodicities for D_{50} **(Fig. 11)**. The 24 kyr periodicity was found to be closely related to the Earth's precessional cycle (~23 kyr). This corresponds well with the Fe_{MAR} record and illustrates the strong orbital control on the source area aridity and dust deposition. The 23 kyr periodicity has been recorded in many Arabian Sea monsoonal records (Sirocko et.al., 1996; Clemens and Prell, 2003; Yu et al., 2019). The 12810 yr periodicity observed in the D_{50} is the second harmonic of precession cycle (Clemens and Prell, 1990). The 757 year periodicity is close to the ~750 year cycle commonly observed in the sediment records of South Asian monsoon regime (Sarkar et al., 2000; Staubwasser, 2003; Thamban et al., 2007; von Rad et al., 1999) and suggested to be related to the variations in the oceanic thermohaline circulation, specifically, the changes in the North Atlantic Deep Water (NADW) formation that control incorporation of ^{14}C into the ocean (Neff et al., 2001 and the references therein). The periodicities of 1274 year in the S-ratio and 1433 yr in the D_{50} of GC2 record are close to the ~1470 year (±20%) pacing of Dansgaard-Oeschger warm events (Schulz, 2002) and validates our interpretation that the northern hemisphere oscillations control the EAS climate on millennial timescales.

5. Conclusions

A sediment core SSK80/GC2 collected from a bathymetric high in the Eastern Arabian Sea tracks the eolian sedimentation for the past 50 kyr and was used to infer the source area aridity and the SW monsoon wind strength of the past. The present record of environmental magnetic parameter S-ratio, used here as a proxy of mineral dust deposition, correlates well with the $\delta^{18}O$ record from the Greenland ice core (GISP2) and is synchronous to the northern hemisphere climatic oscillations such as Dansgaard–Oeschger and Heinrich events in the EAS. The warm D/O events are marked by increased S-ratios (high dust deposition) indicating the increased summer monsoon wind strength while the cold Heinrich events are marked by decreased S-ratios (reduced dust deposition) responding to the reduced wind strength. The mass accumulation of Mg and Fe, diagnostic of source area aridity, reveals high values during 29 - 18 kyr reflecting the increased source area aridity and dust transport during the last glacial period and correlates positively with the global ice volume and insolation records. The spectral analysis of the S-ratio record (dust deposition) reveals significant periodicities centered at 24 kyr, 1274 yr and 757 yr. While the 24 kyr periodicity is the orbital precession cycle of the Earth and typically a predominant monsoon cycle, 1274 year periodicity would represent Dansgaard-Oeschger warm events and the 757 yr periodicity is linked to the North Atlantic deep water formation.

Data availability

Full data used in this paper is made available as a supplementary file

Acknowledgements

Authors are thankful to the Directors of CSIR – NIO, Goa and CSIR – NGRI, Hyderabad for the permissions and support. Dr. V.K. Banakar is acknowledged for his help in ICP – OES analysis. We thank Ship Cell, NIO, and the crew members of RV Sindhu Sankalp for helping us collect the sediment core used in this study. We thank Dr. Rahul Mohan of National Centre for Polar and Ocean Research, Goa for providing FE-SEM facility and Ms. Sahina Gazi for SEM and EDS analyses. We thank Aswini M.A. for her help in preparing the location map. TS is thankful to CSIR-Shyama Prasad Mukherjee Fellowship (SPMF) for providing the research fellowship. Two anonymous reviewers and handling Editor Dr. Adina Paytan are thanked for very constructive reviews. This work is a contribution to CSIR XII Plan project GEOSINKS (PSC0106). This is CSIR -NIO's contribution No.XXXX.

Author statement

Conceptualization - TS and BNN, Investigation - TS, MBL, MV, TM, DJR, SK and LP, Data Curation - TS and BNN, Writing - Original Draft - TS, Writing - Review & Editing - BNN, Resources and Funding acquisition – BNN

References

Agnihotri, R., Sarin, M.M., Somayajulu, B.L.K., Jull, A.J.T., Burr, G.S., 2003. Late-Quaternary biogenic productivity and organic carbon deposition in the eastern Arabian Sea. Palaeogeogr Palaeoclimatol Palaeoecol 197, 43–60. https://doi.org/10.1016/S0031-0182(03)00385-7

Allen, J.R.M., Brandt, U., Brauer, A., Hubberten, H.-W., Huntley, B., Keller, J., Kraml, M., Mackensen, A., Mingram, J., Negendank, J.F.W., Nowaczyk, N.R., Oberhänsli, H., Watts, W.A., Wulf, S., Zolitschka, B., 1999. Rapid environmental changes in southern Europe during the last glacial period. Nature 400, 740–743. https://doi.org/10.1038/23432

Altabet, M.A., Higginson, M.J., Murray, D.W., 2002. The effect of millennial-scale changes in Arabian Sea denitrification on atmospheric CO2. Nature 415, 159–162. https://doi.org/10.1038/415159a

Arz, H.W., Pätzold, J., Wefer, G., 1998. Correlated Millennial-Scale Changes in Surface Hydrography and Terrigenous Sediment Yield Inferred from Last-Glacial Marine Deposits off Northeastern Brazil. Quat Res 50, 157–166.

Bali, K., Mishra, A.K., Singh, S., Chandra, S., Lehahn, Y., 2019. Impact of dust storm on phytoplankton bloom over the Arabian Sea: a case study during March 2012. Environmental Science and Pollution Research 26, 11940–11950. https://doi.org/10.1007/S11356-019-04602-7/FIGURES/7

Banerjee, P., Prasanna Kumar, S., 2014. Dust-induced episodic phytoplankton blooms in the Arabian Sea during winter monsoon. J Geophys Res Oceans 119, 7123–7138. https://doi.org/10.1002/2014JC010304

Bender, M., Sowers, T., Dickson, M.-L., Orchardo, J., Grootes, P., Mayewski, P.A., Meese, D.A., 1994. Climate correlations between Greenland and Antarctica during the past 100,000 years. Nature 372, 663–666. https://doi.org/10.1038/372663a0

Benson, L. v., Lund, S.P., Burdett, J.W., Kashgarian, M., Rose, T.P., Smoot, J.P., Schwartz, M., 1998. Correlation of Late-Pleistocene Lake-Level Oscillations in Mono Lake, California, with North Atlantic Climate Events. Quat Res 49, 1–10. https://doi.org/10.1006/qres.1997.1940

Berger, A., Loutre, M.F., 1991. Insolation values for the climate of the last 10 million years. Quat Sci Rev 10, 297–317. https://doi.org/10.1016/0277-3791(91)90033-Q

Bijesh, C.M., John Kurian, P., Yatheesh, V., Tyagi, A., Twinkle, D., 2018. Morphotectonic characteristics, distribution and probable genesis of bathymetric highs off southwest coast of India. Geomorphology 315, 33–44. https://doi.org/10.1016/J.GEOMORPH.2018.04.015

Bloemendal, J., King, J.W., Hunt, A., Demenocal, P.B., Hayashida, A., 1993. Origin of the sedimentary magnetic record at Ocean Drilling Program Sites on the Owen Ridge, western Arabian Sea. J Geophys Res 98, 4199. https://doi.org/10.1029/92JB02914

Burns, S.J., Fleitmann, D., Matter, A., Kramers, J., Al-Subbary, A.A., 2003. Indian Ocean Climate and an Absolute Chronology over Dansgaard/Oeschger Events 9 to 13. Science (1979) 301, 1365–1367.

Cacho, I., Grimalt, J.O., Pelejero, C., Canals, M., Sierro, F.J., Flores, J.A., Shackleton, N., 1999. Dansgaard-Oeschger and Heinrich event imprints in Alboran Sea paleotemperatures. Paleoceanography 14, 698–705. https://doi.org/10.1029/1999PA900044

Charles, C.D., Lynch-Stieglitz, J., Ninnemann ', U.S., Fairbanks, R.G., 1996. Climate connections between the hemisphere revealed by deep sea sediment core/ice core correlations. Earth Planet Sci Lett 142, 19–27.

Chaubey, A.K., Gopala Rao, D., Srinivas, K., Ramprasad, T., Ramana, M.V., Subrahmanyam, V., 2002. Analyses of multichannel seismic reflection, gravity and magnetic data along a regional profile across the central-western continental margin of India. Mar Geol 182, 303–323. https://doi.org/10.1016/S0025-3227(01)00241-9

Clemens, S.C., 1998. Dust response to seasonal atmospheric forcing: Proxy evaluation and calibration. Paleoceanography 13, 471–490. https://doi.org/10.1029/98PA02131

Clemens, S.C., Prell, W.L., 1990. Late Pleistocene variability of Arabian Sea summer monsoon winds and continental aridity: Eolian records from the lithogenic component of deep-sea sediments. Paleoceanography 5, 109–145. https://doi.org/10.1029/PA005I002P00109

Clemens, S.C., Prell, W.J., 1991. One million year record of summer monsoon winds and continental aridity from the Owen Ridge (Site 722), Northwest Arabian Sea, Proceedings of the Ocean Drilling Program, Scientific Results.

Clemens, S.C., Prell, W.L., 2003. A 350,000 year summer-monsoon multi-proxy stack from the Owen Ridge, Northern Arabian Sea. Mar Geol 201, 35–51. https://doi.org/10.1016/S0025-3227(03)00207-X

Clift, P.D., Giosan, L., Blusztajn, J., Campbell, I.H., Allen, C., Pringle, M., Tabrez, A.R., Danish, M., Rabbani, M.M., Alizai, A., Carter, A., Lückge, A., 2008. Holocene erosion of the Lesser Himalaya triggered by intensified summer monsoon. Geology 36, 79–82. https://doi.org/10.1130/G24315A.1

Dansgaard, W., Johnsen, S.J., Clausen, H.B., Dahl-Jensen, D., Gundestrup, N.S., Hammer, C.U., Hvidberg, C.S., Steffensen, J.P., Sveinbjörnsdottir, A.E., Jouzel, J., Bond, G., 1993. Evidence for general instability of past climate from a 250-kyr ice-core record. Nature 364, 218–220. https://doi.org/10.1038/364218a0

Dearing, J.A., Dann, R.J.L., Hay, K., Lees, J.A., Loveland, P.J., Maher, B.A., O'Grady, K., 1996. Frequency-dependent susceptibility measurements of environmental materials. Geophys J Int 124, 228–240. https://doi.org/10.1111/J.1365-246X.1996.TB06366.X

Dearing, J.A., Bird, P.M., Dann, R.J.L., Benjamin, S.F., 1997. Secondary ferrimagnetic minerals in Welsh soils: a comparison of mineral magnetic detection methods and implications for mineral formation. Geophys J Int 130, 727–736. https://doi.org/10.1111/j.1365-246X.1997.tb01867.x

Debrabant, P., Krissek, L.A., Bouquillon, A., Chamley, H., 1991. Clay mineralogy of Neogene sediments of the western Arabian Sea: mineral abundances and paleoenvironmental implications. Proceedings of the Ocean Drilling Program, Scientific Results 117, 183–196.

Deplazes, G., Lückge, A., Stuut, J.-B.W., Pätzold, J., Kuhlmann, H., Husson, D., Fant, M., Haug, G.H., (2014). Weakening and strengthening of the Indian monsoon during Heinrich events and Dansgaard-Oeschger oscillations. Paleoceanography 29, 99–114. https://doi.org/10.1002/2013PA002509

Dinarès-Turell, J., Hoogakker, B.A.A., Roberts, A.P., Rohling, E.J., Sagnotti, L., 2003. Quaternary climatic control of biogenic magnetite production and eolian dust input in cores from the Mediterranean Sea. Palaeogeogr Palaeoclimatol Palaeoecol 190, 195–209. https://doi.org/10.1016/S0031-0182(02)00605-3

Dorfman, J.M., Stoner, J.S., Finkenbinder, M.S., Abbott, M.B., Xuan, C., St-Onge, G., 2015. A 37,000-year environmental magnetic record of aeolian dust deposition from Burial Lake, Arctic Alaska. Quat Sci Rev 128, 81–97. https://doi.org/10.1016/j.quascirev.2015.08.018

Dutta, K., 2008. Marine ^{14}C reservoir ages and Suess effect in the Indian Ocean. India Earth Sci. 1 (IV), 243e257

Govil, P., Naidu, P.D., 2010. Evaporation-precipitation changes in the eastern Arabian Sea for the last 68 ka: Implications on monsoon variability. Paleoceanography 25, 1210. https://doi.org/10.1029/2008PA001687

Gowan, E.J., Zhang, X., Khosravi, S., Rovere, A., Stocchi, P., Hughes, A.L.C., Gyllencreutz, R., Mangerud, J., Svendsen, J.I., Lohmann, G., 2021. A new global ice sheet reconstruction for the past 80 000 years. Nature Communications 2021 12:1 12, 1–9. https://doi.org/10.1038/s41467-021-21469-w

Grootes, P.M., Stuiver, M., 1997. Oxygen 18/16 variability in Greenland snow and ice with 10−3- to 105-year time resolution. J Geophys Res Oceans 102, 26455–26470. https://doi.org/10.1029/97JC00880

Heinrich, H., 1988. Origin and consequences of cyclic ice rafting in the Northeast Atlantic Ocean during the past 130,000 years. Quat Res 29, 142–152. https://doi.org/10.1016/0033-5894(88)90057-9

Jaglan, S., Gupta, A. K., Clemens, S. C., Dutt, S., Cheng, H., & Singh, R. K. (2021). Abrupt Indian summer monsoon shifts aligned with Heinrich events and D-O cycles since MIS 3. Palaeogeography, Palaeoclimatology, Palaeoecology, 583, 110658. https://doi.org/10.1016/j.palaeo.2021.110658

Jickells, T.D., An, Z.S., Andersen, K.K., Baker, A.R., Bergametti, C., Brooks, N., Cao, J.J., Boyd, P.W., Duce, R.A., Hunter, K.A., Kawahata, H., Kubilay, N., LaRoche, J., Liss, P.S., Mahowald, N., Prospero, J.M., Ridgwell, A.J., Tegen, I., Torres, R., 2005. Global Iron Connections between Desert Dust, Ocean Biogeochemistry, and Climate. Science (1979) 308, 67–71. https://doi.org/10.1126/SCIENCE.1105959

Karlin, R., 1990. Magnetite diagenesis in marine sediments from the Oregon continental margin. J Geophys Res 95, 4405. https://doi.org/10.1029/JB095iB04p04405

Krissek, L.A., Clemens, S.C., 1992. Evidence for aridity-driven dust flux to the northwest Arabian Sea and for decoupling of the dust and upwelling systems. Geological Society, London, Special Publications 64, 359–378. https://doi.org/10.1144/GSL.SP.1992.064.01.24

Leuschner, D. C., Sirocko, F. (2000). The low-latitude monsoon climate during Dansgaard–Oeschger cycles and Heinrich Events. Quaternary Science Reviews, 19(1-5), 243-254. https://doi.org/10.1016/S0277-3791(99)00064-5

Leuschner, D.C., Sirocko, F., Schettler, G., Garbe-Schönberg, D. (2004). Geochemical implications for changing dust supply by the Indian Monsoon system to the Arabian Sea during the last glacial cycle. In: Smykatz-Kloss, W., Felix-Henningsen, P. (eds) Paleoecology of Quaternary Drylands. Lecture Notes in Earth Sciences, vol 102. Springer, Berlin, Heidelberg. https://doi.org/10.1007/978-3-540-44930-0_8

Linsy, P., Nagender Nath, B., Mascarenhas-Pereira, M.B.L., Vinitha, P.V., Ray, D., Prakash Babu, C., Ramalingeswara Rao, B., Kazip, A., Sebastian, T., Kocherla, M., Miriyala, P., 2018. Benthic cycling of phosphorus in the Eastern Arabian Sea: Evidence of present day phosphogenesis. Mar Chem 199, 53–66.

Maher, B. A., 1998. Magnetic properties of modern soils and Quaternary loessic paleosols: paleoclimatic implications. Palaeogeogr Palaeoclimatol Palaeoecol 137, 25–54. https://doi.org/10.1016/S0031-0182(97)00103-X

Mir, I.A., Mascarenhas, M.B.L., Khare, N., 2022. Geochemistry and granulometry as indicators of paleoclimate, weathering, and provenance of sediments for the past 1,00,000 years in the eastern Arabian Sea. J Asian Earth Sci 227, 105102. https://doi.org/10.1016/J.JSEAES.2022.105102

Miriyala, P., Sukumaran, N.P., Nath, B.N., Ramamurty, P.B., Sijinkumar, A. v., Vijayagopal, B., Ramaswamy, V., Sebastian, T., 2017. Increased chemical weathering during the deglacial to mid-Holocene summer monsoon intensification. Scientific Reports 2017 7:1 7, 1–11. https://doi.org/10.1038/srep44310

Nagoji, S., Tiwari, M., 2021. Causes and climatic influence of centennial-scale denitrification variability in the southeastern Arabian Sea since the last glacial period. Quaternary Research (United States) 101, 156–168. https://doi.org/10.1017/QUA.2020.118

Naqvi, S., Jayakumar, D., Narvekar, P., Nature, H.N.-, 2000, U., 2000. Increased marine production of N_2O due to intensifying anoxia on the Indian continental shelf. Nature 408, 346–349.

Narvekar, J., D'Mello, J.R., Prasanna Kumar, S., Banerjee, P., Sharma, V., Shenai-Tirodkar, P., 2017. Winter-time variability of the eastern Arabian Sea: A comparison between 2003 and 2013. Geophys Res Lett 44, 6269–6277. https://doi.org/10.1002/2017GL072965

Neff, U., Burns, S.J., Mangini, A., Mudelsee, M., Fleitmann, D., Matter, A., 2001. Strong coherence between solar variability and the monsoon in Oman between 9 and 6 kyr ago. Nature 411, 290–293. https://doi.org/10.1038/35077048

Nimmy, P.M., Rao, N.R., Neelavannan, K., Hussain, S.M., Mahapatra, S.R., 2021. The coupling of Orbulina universa diameter with the warming and cooling events in the Arabian Sea over the past 40,000 years. Curr Sci 120.

Oldfield, F., 1991. Environmental magnetism — A personal perspective. Quat Sci Rev 10, 73–85. https://doi.org/10.1016/0277-3791(91)90031-O

Peterson, L.C., Haug, G.H., Hughen, K.A., Röhl, U., 2000. Rapid changes in the hydrologic cycle of the tropical Atlantic during the last glacial. Science 290, 1947–51. https://doi.org/10.1126/SCIENCE.290.5498.1947

Porter, S.C., Zhisheng, A., 1995. Correlation between climate events in the North Atlantic and China during the last glaciation. Nature 375, 305–308. https://doi.org/10.1038/375305a0

Pourmand, A., Marcantonio, F., Schulz, H., 2004. Variations in productivity and eolian fluxes in the northeastern Arabian Sea during the past 110 ka. Earth Planet Sci Lett 221, 39–54. https://doi.org/10.1016/S0012-821X(04)00109-8

Prins, M.A., Weltje, G.J., 1999. End-Member Modeling of Siliciclastic Grain-Size Distributions: The Late Quaternary Record of Eolian and Fluvial Sediment Supply to the Arabian Sea and its Paleoclimatic Significance. Numerical Experiments in Stratigraphy: Recent Advances in Stratigraphic and Sedimentologic Computer Simulations, John W. Harbaugh, W. Lynn Watney, Eugene C. Rankey, Rudy Slingerland, Robert H. Goldstein, Evan K. Franseen https://doi.org/10.2110/PEC.99.62.0091

Ramaswamy, V., Muraleedharan, P.M., Prakash Babu, C., 2017. Mid-troposphere transport of Middle-East dust over the Arabian Sea and its effect on rainwater composition and sensitive ecosystems over India. Sci Rep 7. https://doi.org/10.1038/s41598-017-13652-1

Rao, D.G., Paropkari, A.L., Krishna, K.S., Chaubey, A.K., Ajay, K.K., Kodagali, V.N., 2010. Bathymetric highs in the mid-slope region of the western continental margin of India—Structure and mode of origin. Mar Geol 276, 58–70. https://doi.org/10.1016/j.margeo.2010.07.007

Rea, D.K., 1994. The paleoclimatic record provided by eolian deposition in the deep sea: The geologic history of wind. Reviews of Geophysics 32, 159–195. https://doi.org/10.1029/93RG03257

Reichart, G.J., den Dulk, M., Visser, H.J., van der Weijden, C.H., Zachariasse, W.J., 1997. A 225 kyr record of dust supply, paleoproductivity and the oxygen minimum zone from the Murray Ridge (northern Arabian Sea). Palaeogeogr Palaeoclimatol Palaeoecol 134, 149–169. https://doi.org/10.1016/S0031-0182(97)00071-0

Rowan, C.J., Roberts, A.P., Broadbent, T., 2008. Reductive diagenesis, magnetite dissolution, greigite growth and paleomagnetic smoothing in marine sediments: A new view. Earth Planet Sci Lett 277, 223–235. https://doi.org/10.1016/j.epsl.2008.10.016

Sarkar, A., Ramesh, R., Somayajulu, B.L.K., Agnihotri, R., Jull, A.J.T., Burr, G.S., 2000. High resolution Holocene monsoon record from the eastern Arabian Sea. Earth Planet Sci Lett 177, 209–218. https://doi.org/10.1016/S0012-821X(00)00053-4

Schnetger, B., Brumsack, H.J., Schale, H., Hinrichs, J., Dittert, L., 2000. Geochemical characteristics of deep-sea sediments from the Arabian Sea: A high-resolution study. Deep Sea Res 2 Top Stud Oceanogr 47, 2735–2768. https://doi.org/10.1016/S0967-0645(00)00047-3

Schulte, S., Müller, P., 2001. Variations of sea surface temperature and primary productivity during Heinrich and Dansgaard-Oeschger events in the northeastern Arabian Sea. Geo-Marine Letters 21, 168–175. https://doi.org/10.1007/s003670100080

Schulz, H., von Rad, U., Erlenkeuser, H., von Rad, U., 1998. Correlation between Arabian Sea and Greenland climate oscillations of the past 110,000 years. Nature 393, 54–57. https://doi.org/10.1038/31750

Schulz, M., 2002. On the 1470-year pacing of Dansgaard-Oeschger warm events. Paleoceanography 17, 4-1-4–9. https://doi.org/10.1029/2000PA000571

Schulz, M., Mudelsee, M., 2002. REDFIT: estimating red-noise spectra directly from unevenly spaced paleoclimatic time series. Comput Geosci 28, 421–426. https://doi.org/10.1016/S0098-3004(01)00044-9

Sebastian, T., Nagender Nath, B., Venkateshwarlu, M., Miriyala, P., Prakash, A., Linsy, P., Kocherla, M., Kazip, A., Sijinkumar, A.V., 2019. Impact of the Indian Summer Monsoon variability on the source area weathering in the Indo-Burman ranges during the last 21 kyr – A sediment record from the Andaman Sea. Palaeogeogr Palaeoclimatol Palaeoecol 516, 22–34. https://doi.org/10.1016/J.PALAEO.2018.11.035

Sebastian, T., Nath, B.N., Miriyala, P., Linsy, P., Kocherla, M., 2023. Climatic control on detrital sedimentation in the continental margin off Chennai, western Bay of Bengal – A 42 kyr record. Palaeogeography, Palaeoclimatology, Palaeoecology, 609, 111313. https://doi.org/10.1016/j.palaeo.2022.111313

Shimmield, G.B., Mowbray, S.R., Weedon, G.P., 1990. A 350 ka history of the Indian Southwest Monsoon—evidence from deep-sea cores, northwest Arabian Sea. Trans R Soc Edinb Earth Sci 81, 289–299. https://doi.org/10.1017/S0263593300020800

Singh, A.D., Jung, S.J.A., Darling, K., Ganeshram, R., Ivanochko, T., Kroon, D., 2011. Productivity collapses in the Arabian Sea during glacial cold phases. Paleoceanography 26, 3210. https://doi.org/10.1029/2009PA001923

Singh, A.D., 2021. Centennial to millennial-scale changes in thermocline ventilation in the Arabian Sea: insights from the pteropod preservation record. Journal of Palaeosciences, 70((1-2), 253–266. https://doi.org/10.54991/jop.2021.18

Singh, D.P., Saraswat, R., Naik, D.K., 2017. Does Glacial-Interglacial Transition Affect Sediment Accumulation in Monsoon-Dominated Regions? Acta Geologica Sinica - English Edition 91, 1079–1094. https://doi.org/10.1111/1755-6724.13325

Sirocko, F., Garbe-Schönberg, D., Devey, C., 2000. Processes controlling trace element geochemistry of Arabian Sea sediments during the last 25,000 years. Glob Planet Change 26, 217–303. https://doi.org/Doi: 10.1016/s0921-8181(00)00046-1

Sirocko, F., Garbe-Schönberg, D., McIntyre, A., Molfino, B., 1996. Teleconnections between the Subtropical Monsoons and High-Latitude Climates During the Last Deglaciation. Science (1979) 272, 526–529. https://doi.org/10.1126/SCIENCE.272.5261.526

Sirocko, F., Lange, H., 1991. Clay-mineral accumulation rates in the Arabian Sea during the late Quaternary. Mar Geol 97, 105–119. https://doi.org/10.1016/0025-3227(91)90021-U

Staubwasser, M., 2003. Climate change at the 4.2 ka BP termination of the Indus valley civilization and Holocene south Asian monsoon variability. Geophys Res Lett 30, 1425. https://doi.org/10.1029/2002GL016822

Suresh, K., Singh, U., Kumar, A., Karri, D., Peketi, A., Ramaswamy, V., 2021. Provenance tracing of long-range transported dust over the Northeastern Arabian Sea during the southwest monsoon. Atmos Res 250, 105377. https://doi.org/10.1016/J.ATMOSRES.2020.105377

Thamban, M., Kawahata, H., Rao, V.P., 2007. Indian summer monsoon variability during the holocene as recorded in sediments of the Arabian Sea: Timing and implications. J Oceanogr 63, 1009–1020. https://doi.org/10.1007/s10872-007-0084-8

Thamban, M., Purnachandra Rao, V., Schneider, R.R., Grootes, P.M., 2001. Glacial to Holocene fluctuations in hydrography and productivity along the southwestern continental margin of India. Palaeogeogr Palaeoclimatol Palaeoecol 165, 113–127. https://doi.org/10.1016/S0031-0182(00)00156-5

Thompson, R., Oldfield, F., 1986. Environmental Magnetism. Springer Netherlands, Dordrecht. https://doi.org/10.1007/978-94-011-8036-8

von Rad, U., Schaaf, M., Michels, K.H., Schulz, H., Berger, W.H., Sirocko, F., 1999. A 5000-yr Record of Climate Change in Varved Sediments from the Oxygen Minimum Zone off Pakistan, Northeastern Arabian Sea. Quat Res 51, 39–53. https://doi.org/10.1006/QRES.1998.2016

Walden, J., 1999. Remanence measurements, in: Walden, J., Oldfield, F., Smith, J. (Eds.), Environmental Magnetism: A Practical Guide. Quaternary Research Association, London, pp. 63–87.

Webster, P., 1987. The elementary monsoon, in: Fein, J.S., Stephens, P.L. (Eds.), Monsoons. John Wiley & Sons, pp. 3–32.

Wyrtki, K., 1973. Physical Oceanography of the Indian Ocean. Springer Berlin Heidelberg, pp. 18–36. https://doi.org/10.1007/978-3-642-65468-8_3

Wyrtki, K., 1971. Oceanographic Atlas of the International Indian Ocean Expedition, National Science Foundation Publication, OCE.

Yu, Z., Colin, C., Wan, S., Saraswat, R., Song, L., Xu, Z., Clift, P., Lu, H., Lyle, M., Kulhanek, D., Hahn, A., Tiwari, M., Mishra, R., Miska, S., Kumar, A., 2019. Sea level-controlled sediment transport to the eastern Arabian Sea over the past 600 kyr: Clay minerals and SrNd isotopic evidence from IODP site U1457. Quat Sci Rev 205, 22–34. https://doi.org/10.1016/J.QUASCIREV.2018.12.006

Figure Captions

Figure 1: The location map of the sediment core SSK80/GC2 and the other major records (93KL and 136 KL) mentioned in this manuscript. a) Quasi-climatology (2003–2014) of the major winds (850 hpa) over the northern Indian Ocean during summer monsoon period (June, July, August and September) along with the average precipitation (2003–2014) for the month of June, July and August derived from the Tropical Rainfall Measuring Mission satellite (modified from Ramaswamy et al., 2017). The major wind systems are the (A) Low-Level Jet (Findlater Jet), (B) the Shamal winds over the Arabian Peninsula, (C) the Red Sea Winds, and (D) the northerly Levar Winds over SW Asia. Major dust source regions providing mineral dust to the northern Indian Ocean are shown in grey. b) Detailed swath bathymetric depth contour map (contour interval 200 m) and location of the core SSK80/GC2 showing the mid-slope/marginal high along with the geophysical transect A-A′ and c) single channel seismic reflection images of profiles A-A′ modified from Rao et al., (2010).

Figure 2: Age model of the core SSK80/GC2 derived from radiocarbon dating with sedimentation rates. The grey envelope represents the dating error. Marine isotopic stages (MIS) are also marked for comparison.

Figure 3: Downcore variation of mineral magnetic parameter S-ratio, weight percentages of Fe and Mg, Ti/Al ratio, median grain size (D_{50}), and foraminiferal oxygen isotope ratios ($\delta^{18}O$) of SSK80/GC2. $\delta^{18}O$ record of Greenland Ice Sheet Project 2 (GISP2) (Grootes and Stuiver, 1997) is also shown for comparison. The shaded intervals indicate the last glacial maximum (LGM), Heinrich events 1 – 5 and the numbers indicate the Dansgaard–Oeschger (D/O) interstadials. Grey vertical shading bars are shown to compare SSK80/GC2 $\delta^{18}O$ data with GISP2 $\delta^{18}O$ record within the dating uncertainties.

Figure 4: Downcore variation of magnetic parameters of core SSK80/GC2; S-ratio, saturated isothermal remanent magnetization (SIRM), susceptibility of anhysteretic remanent magnetization (χ_{arm}) and magnetic grain-size ratios χ_{arm}/SIRM and χ_{arm}/χ_{lf} are shown.

Figure 5: Bivariate plot of χ_{fd}% versus χ_{arm}/SIRM ratio representing the magnetic grain size. The abbreviations read as SP – superparamagnetic grains, SD – single domain grains, MD – multi domain grains, PSD – pseudo single domain grains, SSD - stable single-domain grains.

Figure 6: Downcore variations in particle size distribution in SSK80/GC2. The variations in median grain size (D_{50}), weight percent of sand (>63 μm) fraction and the silt and clay weight percentages in the <63 μm fraction are shown.

Figure 7: The field emission scanning electron microscope (FE SEM) images and their corresponding energy dispersive spectra (EDS) of magnetic extracts from core GC2. The coarse grained titanomagnetite grains of detrital origin and the fine-grained magnetite grains of biogenic origin can be seen.

Figure 8: Downcore variation of the S-ratio record of SSK80/GC2 (this study) presented along with the published records of total organic carbon (TOC) of 136KL in the western Arabian Sea (Schulz et al., 1998), detrital flux of 93KL in Northeastern Arabian Sea (Pourmand et al., 2004) and the $\delta^{18}O$ record of Greenland Ice Sheet Project 2 (GISP2) (Grootes and Stuiver, 1997). The shaded bars at the top represent the marine isotopic stages. The values along with the arrows on the top mark the ^{14}C calibrated ages of SSK80/GC2.

Figure 9: Downcore variation of the mass accumulation rates of (a) iron (Fe_{MAR}), (b) magnesium (Mg_{MAR}) and (c) Ti/Al ratio of the core SSK80/GC2 along with (d) Mg/Al ratio of core SK117/GC08 from the eastern Arabian Sea (Mir et al., 2022) (e) the lithogenic mass accumulation rate (MAR) of RC 27 – 61 from the Owen Ridge, Western Arabian Sea (Clemens and Prell, 1990) and (f) the global

ice volume record (Gowan et al., 2021). The shaded intervals mark the major climatic periods during the last 50 kyr.

Figure 10: Downcore variation of (a) mass accumulation rate of iron (Fe_{MAR}), and (b) median grain size of core SSK80/GC2 plotted along with published records of monsoon strength, dust supply and continental aridity from the Arabian Sea during the last 50 kyr. The published records are (c) the Summer Monsoon strength indicated by the eolian mean grain size record of NIOP492 from Owen Ridge (Prins and Weltje 1999), (d) the relative amount of lithogenic dust from the Central Arabian Region derived by the first principal component (PC1) from the geochemical record of core 70 KL (Leuschner et al., 2004), and (e) continental aridity derived from the end-member modelling of siliciclastic grain-size distribution of NIOP458 from Upper Indus fan (Prins and Weltje 1999) and (f) solar insolation record of July at 15°N (Berger and Loutre, 1991).

Figure 11: Spectral analysis of S-ratio and median grain size (D_{50}) record of SSK80/GC2 with the prominent peaks marked. The red, green, and blue curves indicate confidence levels of 99%, 95%, and 90% respectively. The spectral analysis was carried out using REDFIT program by Schulz and Mudelsee, (2002).

Table 1: Radiocarbon ages from mixed planktic foraminifera *G. ruber and G. sacculifer* for the dated sections of SSK 80/GC2 along with lab reference codes (NSF-Arizona AMS Laboratory, USA and Radiochronology Lab, Laval University, Canada). The measured radiocarbon ages were corrected for a standard ocean reservoir correction of 400 years and were converted into calendar age using CalPal-7 calibration.

Section (cm)	**Lab Reference Number**	**$\delta^{13}C$ (‰)**	**^{14}C age (yr BP)**	**Calibrated calendar age (yr BP)**
2-3	ULA-5394	-	2475 ± 20	2054 ± 40
9-10	AA108322	1.7	3555 ± 24	3390 ± 19
19-20	AA108323	1.7	5483 ± 25	5833 ± 57
35-36	ULA-5395	-	15040 ± 40	17968 ± 375
67=68	ULA-5396	-	21360 ± 50	25078 ± 342
99-100	ULA-5397	-	24600 ± 60	28967 ± 384
119-120	AA108324	1.8	34680 ± 600	39579 ± 970
140-141	ULA-5398	-	43060 ± 160	46026 ± 997

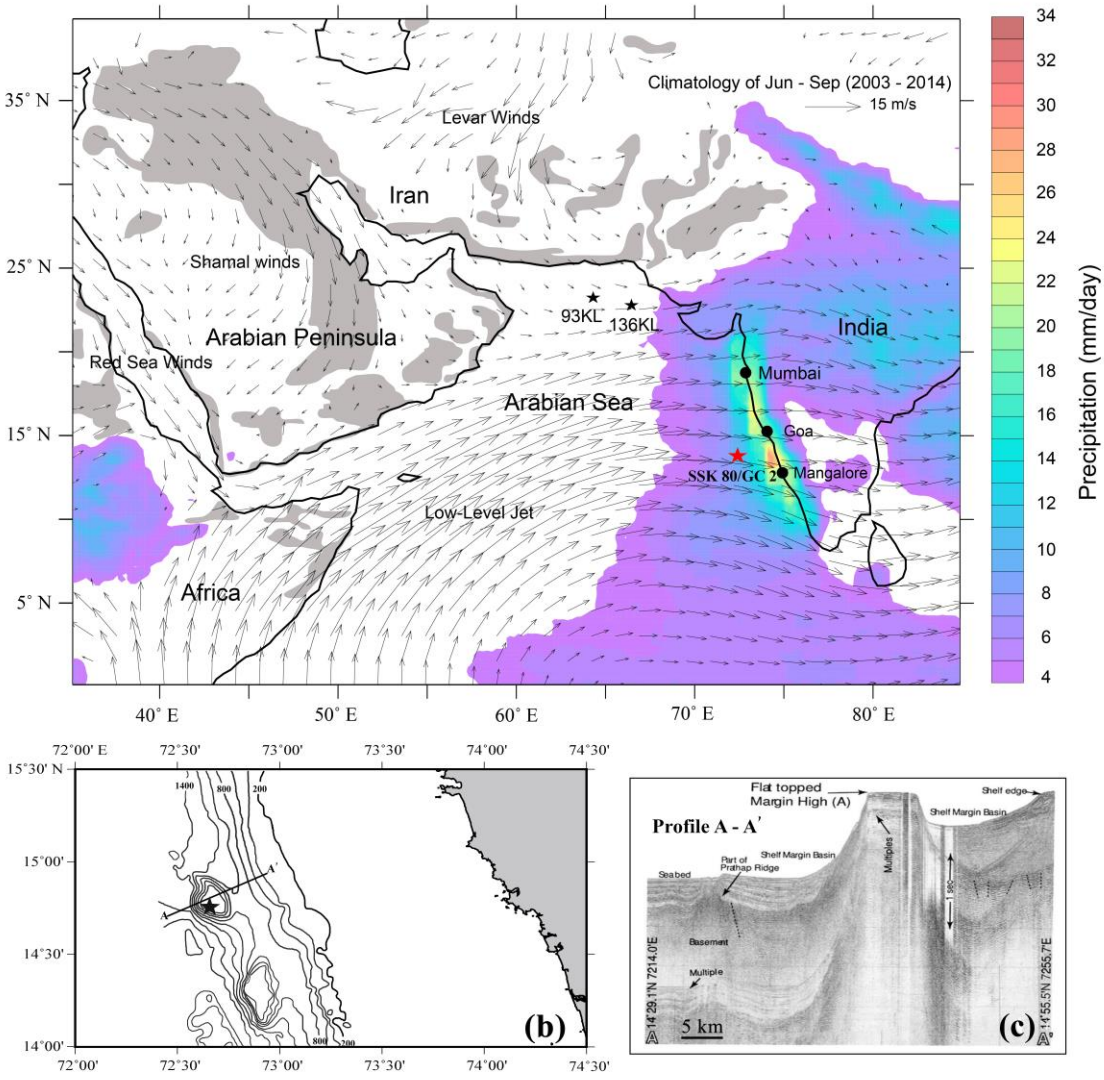
Climatology of Jun - Sep (2003 - 2014)
15 m/s
Levar Winds
Iran
Shamal winds
Arabian Peninsula
Red Sea Winds
93KL
136KL
India
Mumbai
Goa
Mangalore
SSK 80/GC 2
Arabian Sea
Low-Level Jet
Africa
35° N
25° N
15° N
5° N
40° E
50° E
60° E
70° E
80° E
Precipitation (mm/day)
34
32
30
28
26
24
22
20
18
16
14
12
10
8
6
4
72°00' E
72°30'
73°00'
73°30'
74°00'
74°30'
15°30' N
15°00'
14°30'
14°00'
1400
800
200
(b)
Flat topped
Margin High (A)
Profile A - A'
Shelf edge
Shelf Margin Basin
Seabed
Part of
Prathap Ridge
Shelf Margin Basin
Multiples
Basement
Multiple
5 km
(c)

Figure 1

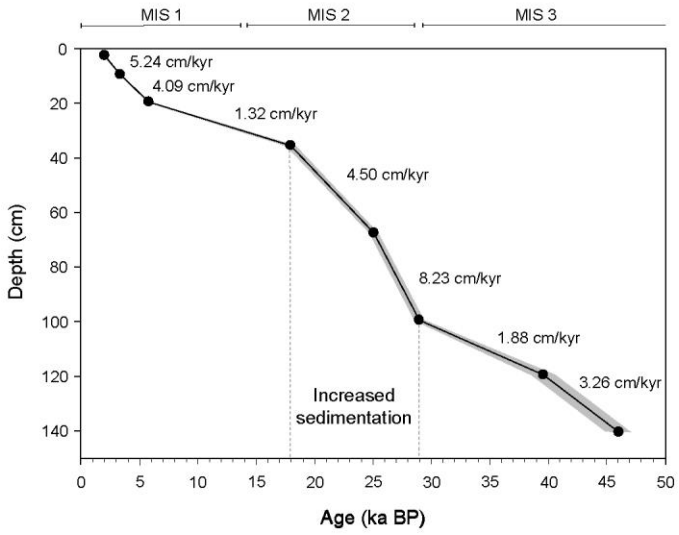
MIS 1
MIS 2
MIS 3
Depth (cm)
0
20
40
60
80
100
120
140
5.24 cm/kyr
4.09 cm/kyr
1.32 cm/kyr
4.50 cm/kyr
8.23 cm/kyr
1.88 cm/kyr
3.26 cm/kyr
Increased sedimentation
0
5
10
15
20
25
30
35
40
45
50
Age (ka BP)

Figure 2

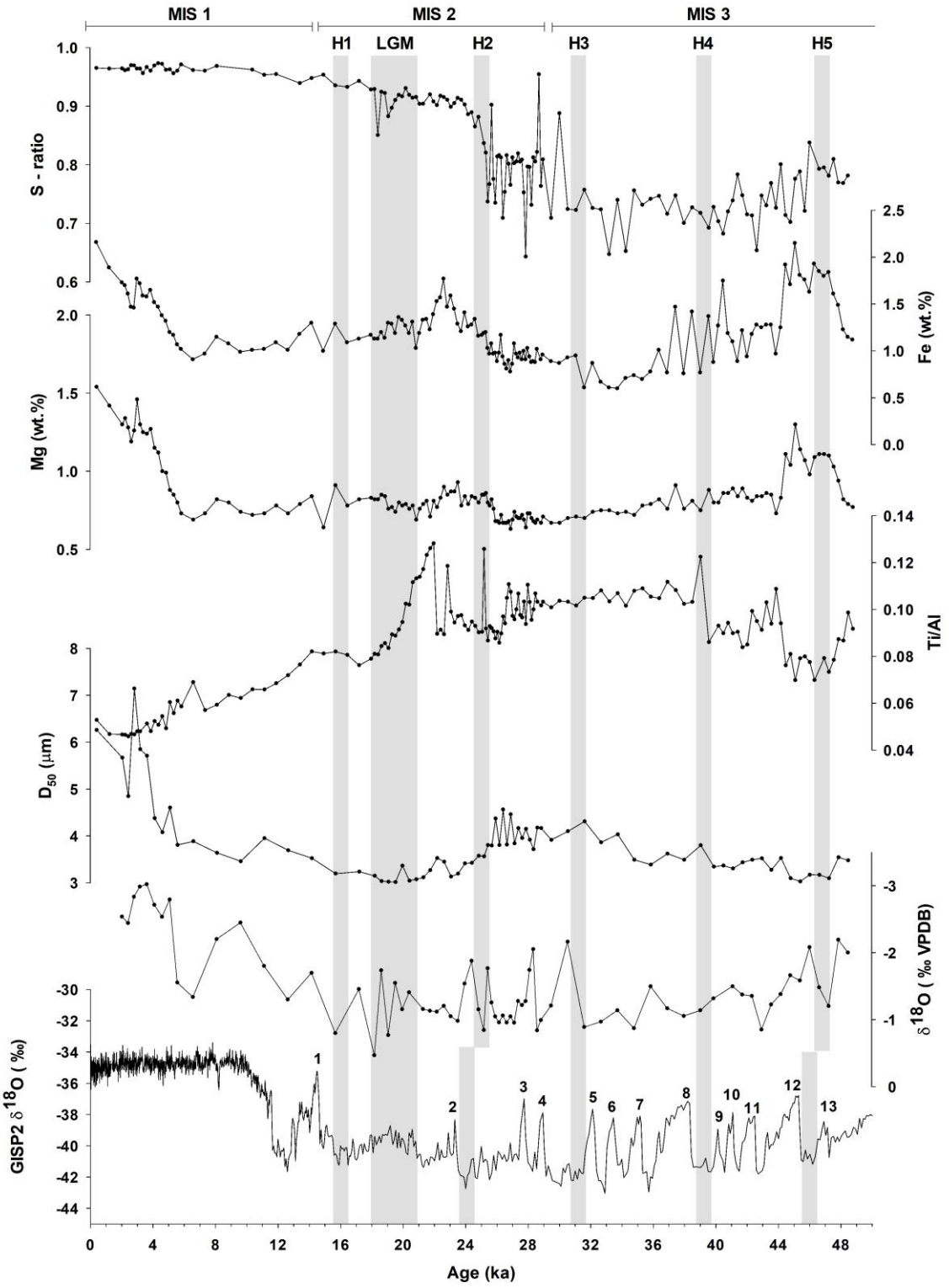
MIS 1
MIS 2
MIS 3
H1
LGM
H2
H3
H4
H5
S - ratio
Mg (wt.%)
Fe (wt.%)
Ti/Al
D_{50} (μm)
$\delta^{18}O$ (‰ VPDB)
GISP2 $\delta^{18}O$ (‰)
Age (ka)
1
2
3
4
5
6
7
8
9
10
11
12
13

Figure 3

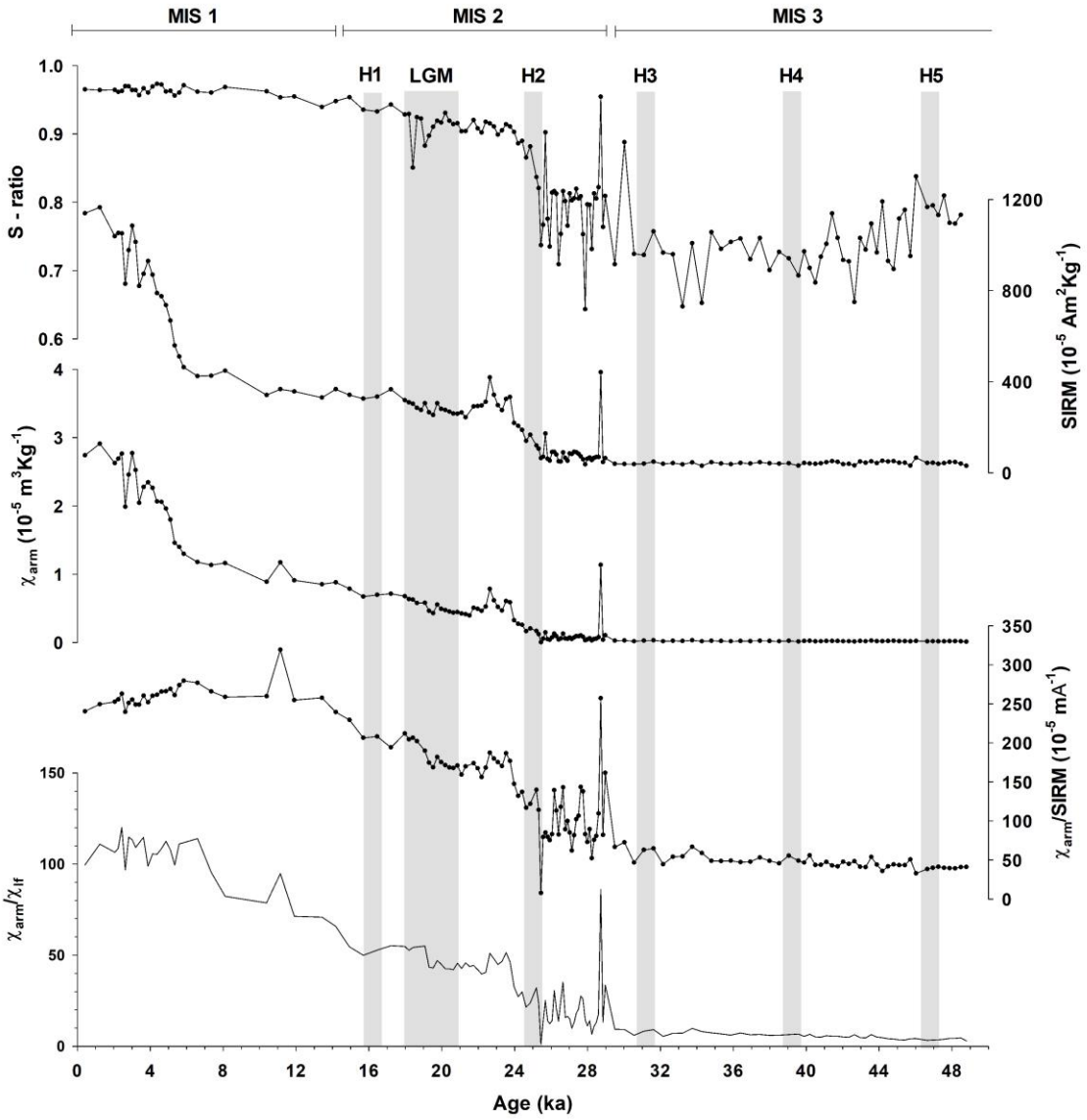
MIS 1
MIS 2
MIS 3
H1
LGM
H2
H3
H4
H5
S - ratio
SIRM (10^{-5} Am^2Kg^{-1})
χ_{arm} (10^{-5} m^3Kg^{-1})
χ_{arm}/SIRM (10^{-5} mA^{-1})
χ_{arm}/χ_{lf}
Age (ka)

Figure 4

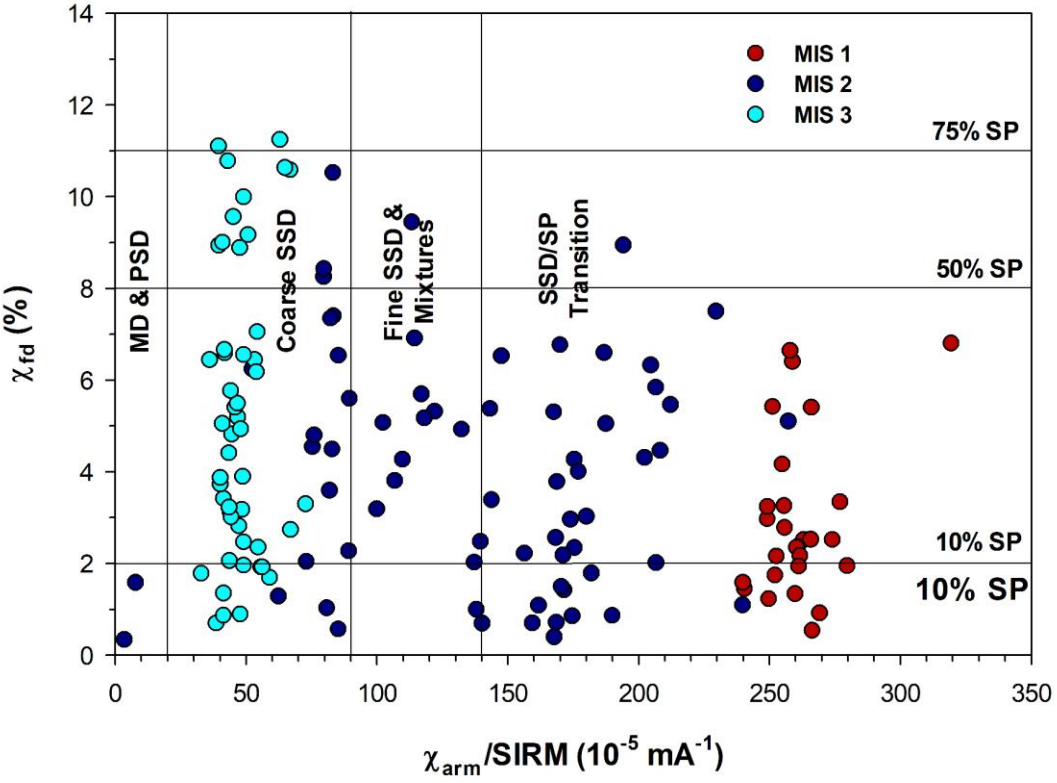
MIS 1
MIS 2
MIS 3
75% SP
50% SP
10% SP
10% SP
MD & PSD
Coarse SSD
Fine SSD & Mixtures
SSD/SP Transition
χfd (%)
χarm/SIRM (10-5 mA-1)
0
2
4
6
8
10
12
14
0
50
100
150
200
250
300
350

Figure 5

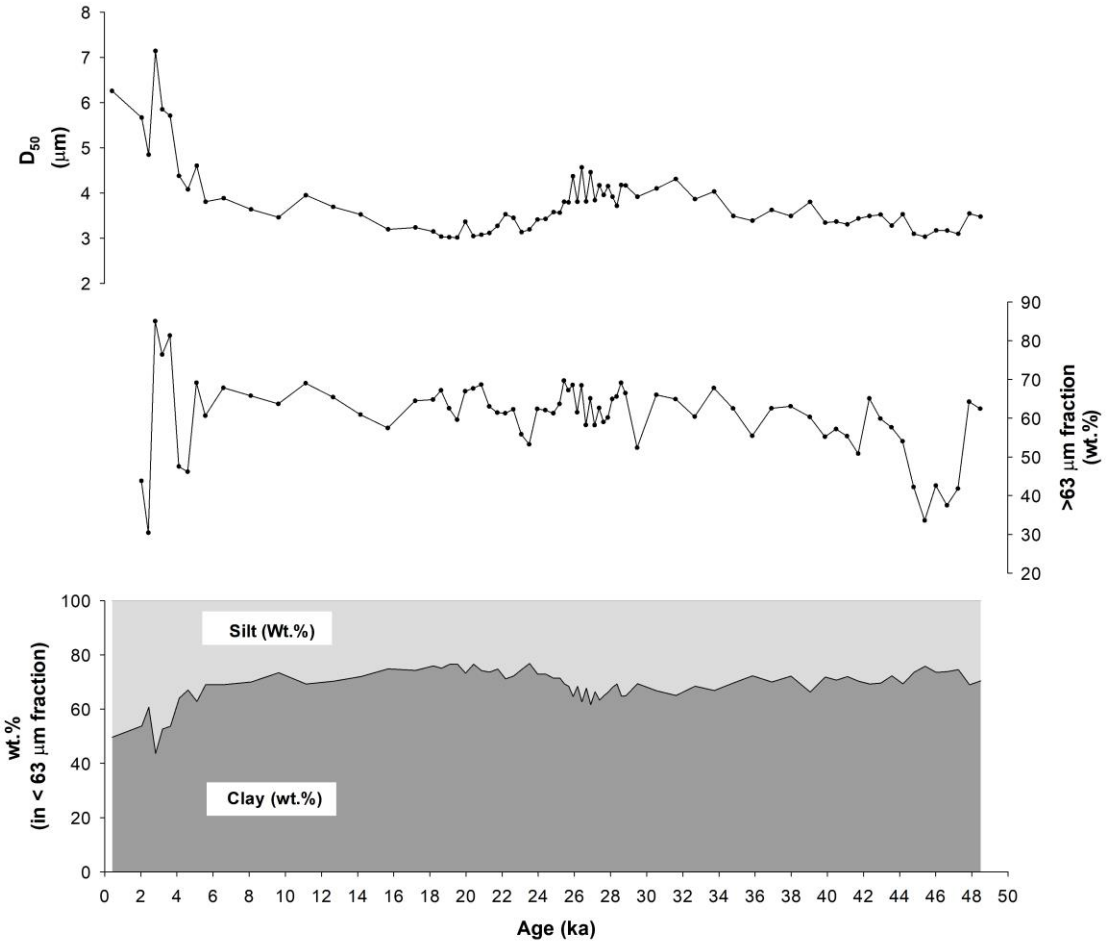
D50 (μm)
>63 μm fraction (wt.%)
wt.% (in < 63 μm fraction)
Silt (Wt.%)
Clay (wt.%)
Age (ka)

Figure 6

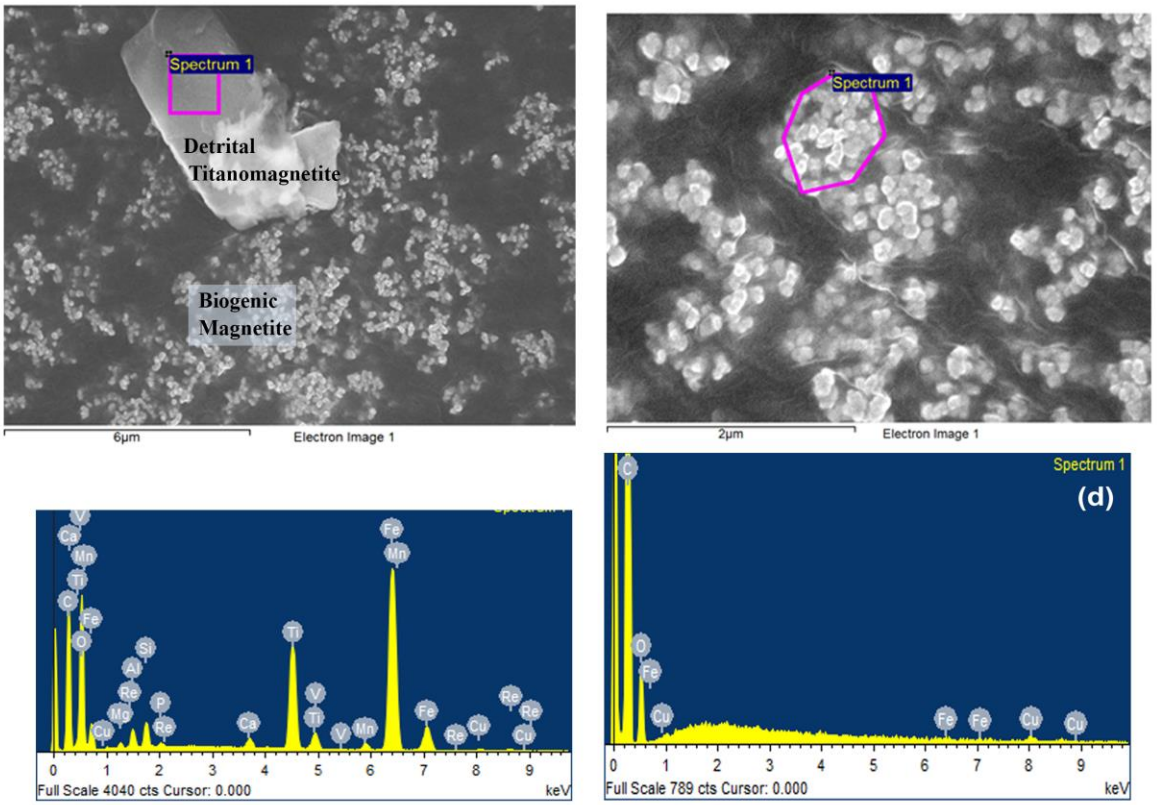
Spectrum 1
Detrital
Titanomagnetite
Biogenic
Magnetite
6µm
Electron Image 1
Spectrum 1
2µm
Electron Image 1
Full Scale 4040 cts Cursor: 0.000
keV
Spectrum 1
(d)
Full Scale 789 cts Cursor: 0.000
keV

Figure 7

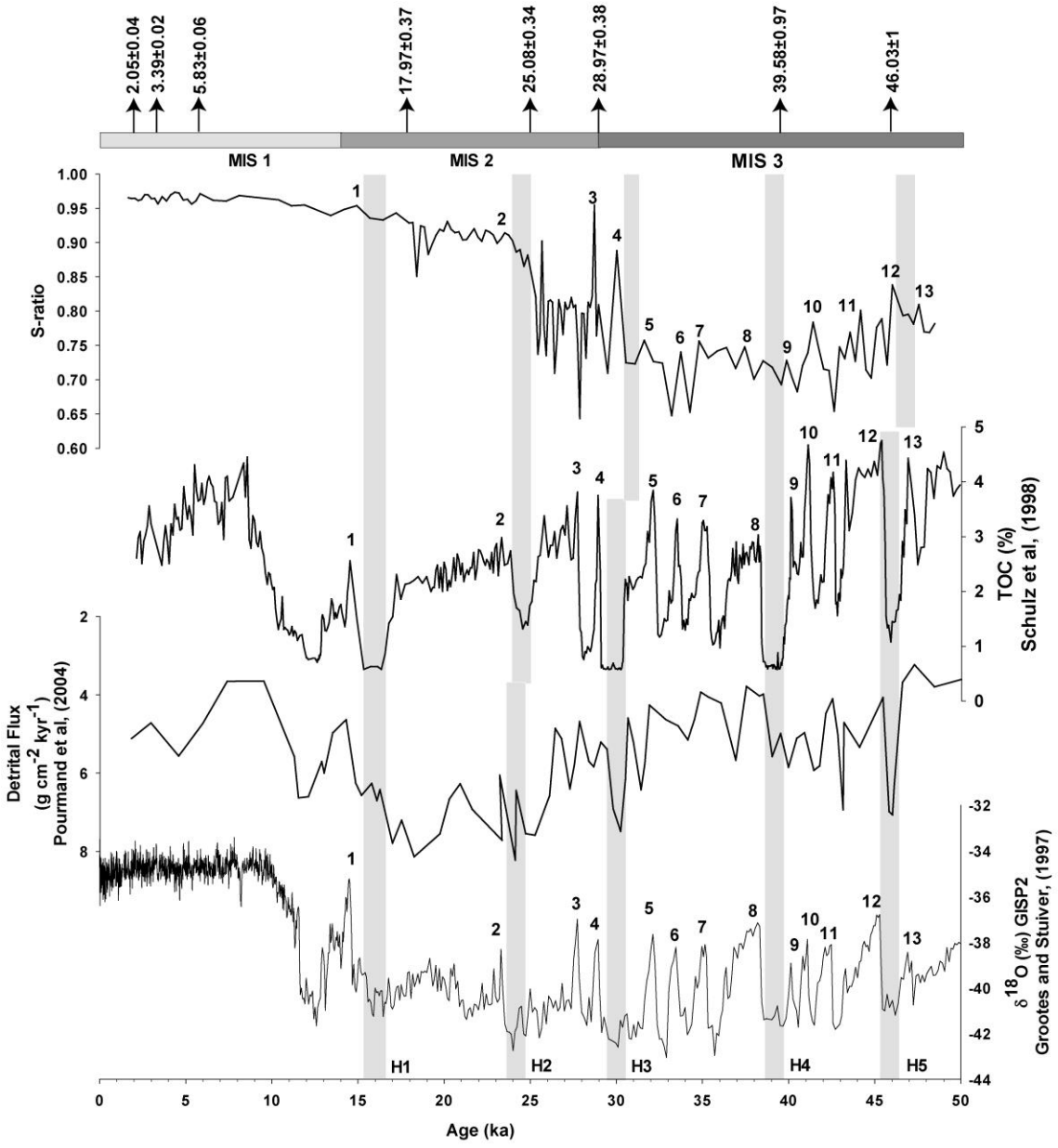
2.05±0.04
3.39±0.02
5.83±0.06
17.97±0.37
25.08±0.34
28.97±0.38
39.58±0.97
46.03±1
MIS 1
MIS 2
MIS 3
S-ratio
TOC (%)
Schulz et al, (1998)
Detrital Flux
(g cm-2 kyr-1)
Pourmand et al, (2004)
δ18O (‰) GISP2
Grootes and Stuiver, (1997)
H1
H2
H3
H4
H5
Age (ka)

Figure 8

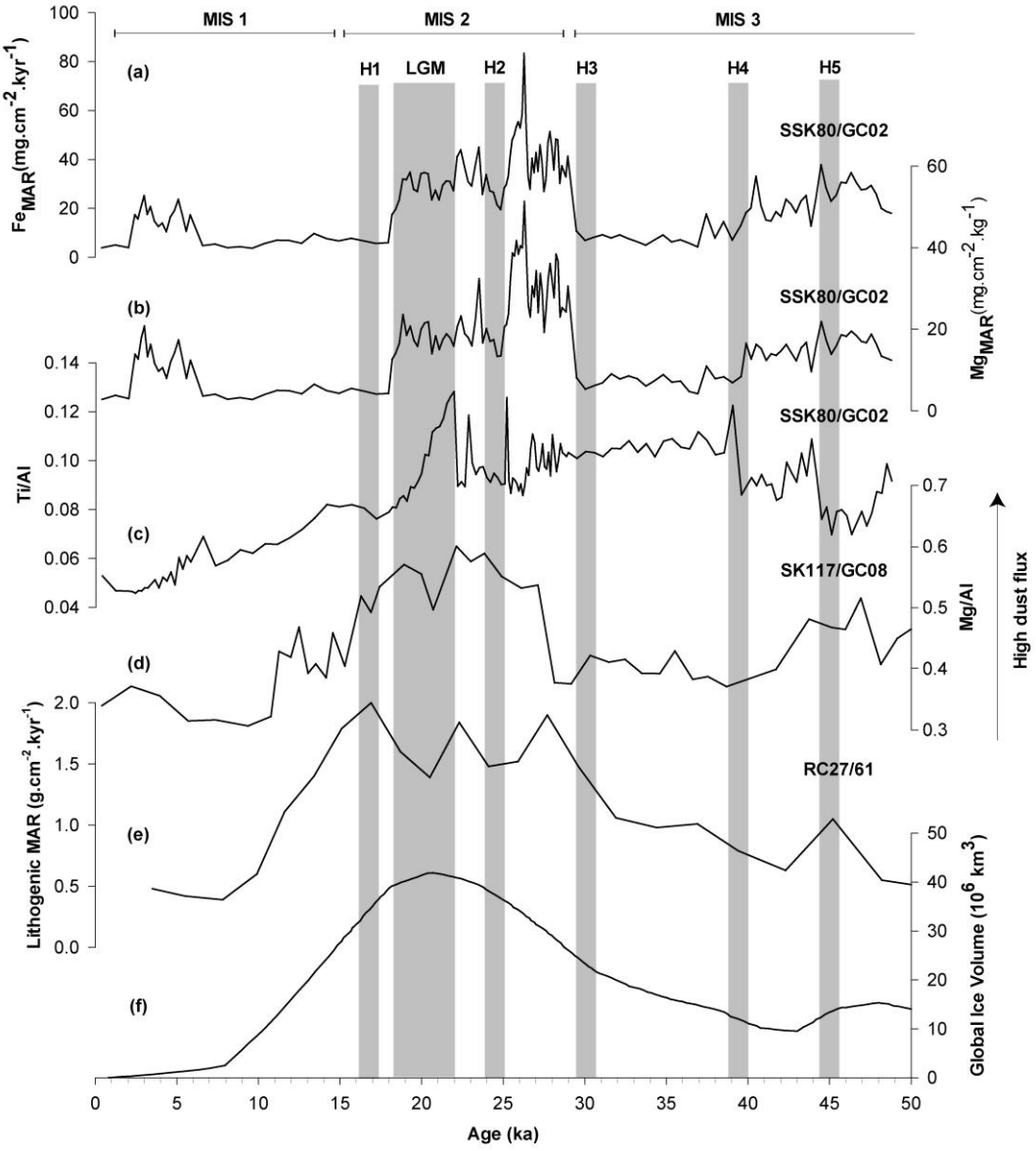
MIS 1
MIS 2
MIS 3
H1
LGM
H2
H3
H4
H5
(a)
SSK80/GC02
(b)
SSK80/GC02
(c)
SSK80/GC02
(d)
SK117/GC08
(e)
RC27/61
(f)
Fe_MAR (mg.cm-2.kyr-1)
Mg_MAR (mg.cm-2.kg-1)
Ti/Al
Mg/Al
High dust flux
Lithogenic MAR (g.cm-2.kyr-1)
Global Ice Volume (10^6 km^3)
Age (ka)

Figure 9

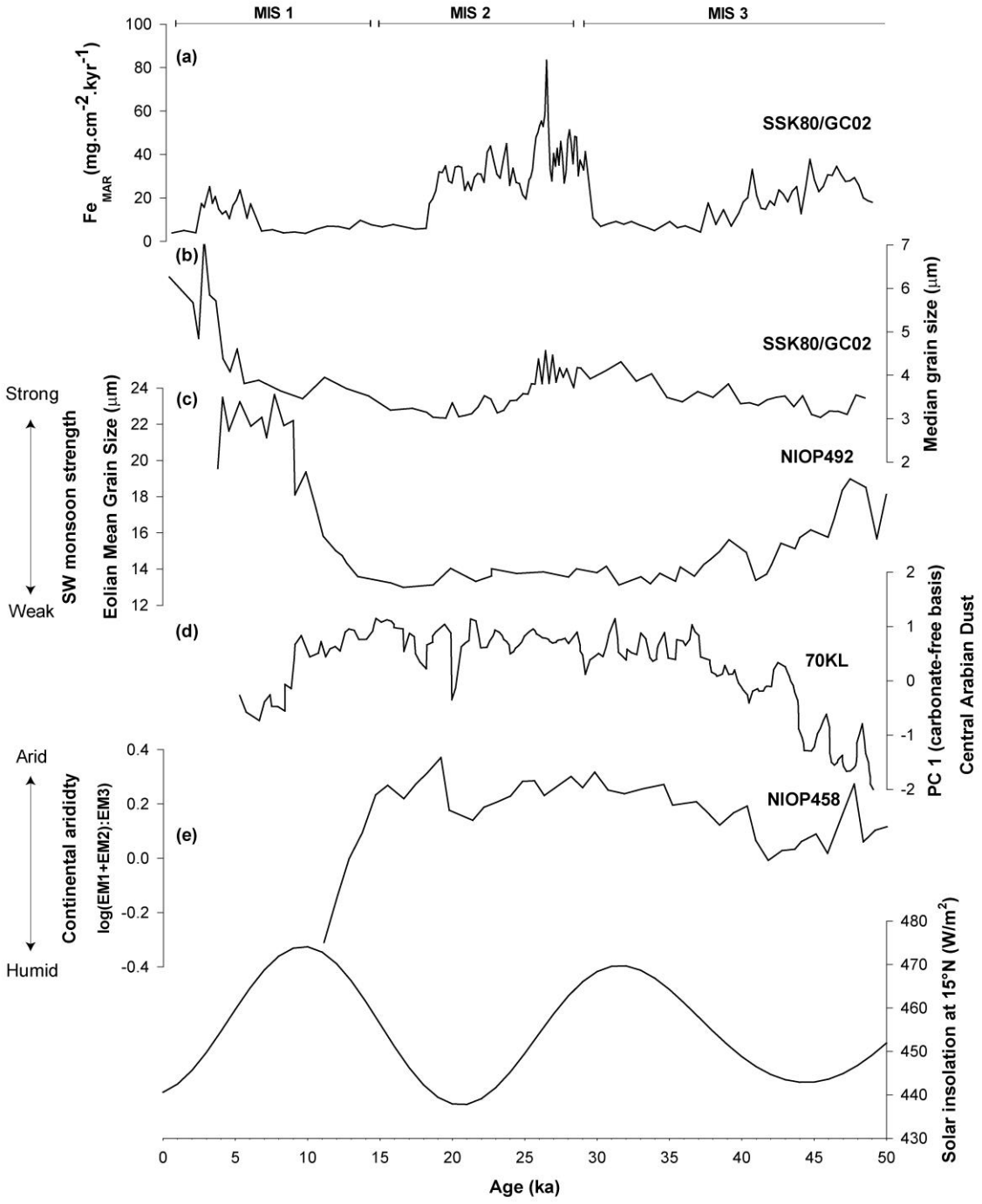
MIS 1
MIS 2
MIS 3
(a)
SSK80/GC02
Fe MAR (mg.cm-2.kyr-1)
(b)
SSK80/GC02
Median grain size (μm)
(c)
NIOP492
Eolian Mean Grain Size (μm)
Strong
Weak
SW monsoon strength
(d)
70KL
PC 1 (carbonate-free basis)
Central Arabian Dust
Arid
Humid
Continental aridity
log(EM1+EM2):EM3)
(e)
NIOP458
Solar insolation at 15°N (W/m2)
Age (ka)

Figure 10

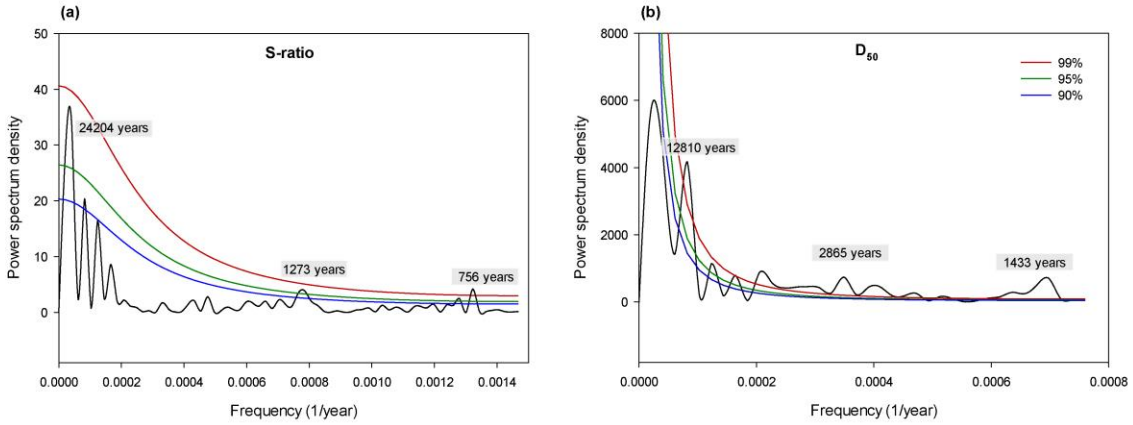
(a)
S-ratio
24204 years
1273 years
756 years
Power spectrum density
Frequency (1/year)
(b)
D50
99%
95%
90%
12810 years
2865 years
1433 years
Power spectrum density
Frequency (1/year)

Figure 11